UNIVERSITY OF CALIFORNIA SAN DIEGO

Physical Properties of Dusty Starburst Cores in Massive Compact Galaxies with Extreme Outflows

A Thesis submitted in partial satisfaction of the
requirements for the degree Master of Science

in

Physics

by

Erin George

Committee in charge:

Professor Alison L Coil, Chair
Professor Quinn Morgan Konopacky
Professor Karin Marie Sandstrom

2020

The Thesis of Erin George is approved, and it is acceptable in quality and form for publication on microfilm and electronically:

_____

_____

_____
Chair

University of California San Diego

2020

TABLE OF CONTENTS

LIST OF FIGURES

LIST OF TABLES

ACKNOWLEDGEMENTS

I would like to acknowledge Dr. Alison Coil for her support throughout this research project. I would also like to acknowledge Dr. Serena Perrotta for her invaluable patience and guidance in helping this project progress and finish.

Both Dr. Coil and Dr. Perrotta are co-authoring a publication with the thesis author in preparation to be submitted later this year. This includes all sections and some of the figures, but with the acquisition of higher quality data that is not present in this thesis.

A large thanks is owed to the HiZEA collaboration for the data used and compiled in Table 1. Additionally, significant gratitude is owed to Dr. Christy Tremonti for the use of her combined MMT/SDSS spectra for our analysis.

ABSTRACT OF THE THESIS

Physical Properties of Dusty Starburst Cores in Massive Compact Galaxies with Extreme Outflows

by

Erin George

Master of Science in Physics

University of California San Diego, 2020

Professor Alison L Coil, Chair

Even though years have been spent studying how star formation is quenched in galaxies, we are still unsure of the physical mechanisms that drive the halt in forming stars. Quenching is presumed to be caused by feedback, which is the expulsion of gas and dust, from various sources inside the galaxy. Unfortunately, feedback is the crux of the current theory of galaxy evolution and how elliptical galaxies are formed. With this in mind, we have gathered a small selection of

unusual late-stage merging galaxies at intermediate redshift. Not only are they very massive, but also compact, bright, blue, still forming stars, and have extremely fast outflows. Using data acquired from Keck/NIRSPEC, the Sloan Digital Sky Survey, and the Multiple Mirror Telescope, we examined forbidden emission lines of these extraordinary galaxies. We found strong indicators of broad line emission tracing the outflow, which is seen in both emission and absorption, indicating the outflows have multiple phases.

1. INTRODUCTION

Elliptical galaxies are currently theorized to be formed through galaxy mergers, although the exact process remains uncertain. A glaring problem with current galaxy evolution theory is that the cosmic baryon fraction predicts a larger stellar mass than what galaxies actually contain (Moster et al. 2013), with the circumgalactic medium (CGM) having a larger fraction of baryons than expected (Werk et al. 2014). Unlike the local universe where all massive galaxies are large, over half of all massive galaxies at $z > 1.5$ are exceptionally compact (e.g., Zirm et al. 2007, van Dokkum et al. 2008, van der Wel et al. 2014). Additional studies have shown that the most likely predecessors of these compact massive galaxies were similarly compact star-forming galaxies, where gas- and dust-rich disk galaxies merged and rapidly quenched (Barro et al. 2013, Sefanon et al. 2013, and van Dokkum et al. 2015). These galaxies are theorized to have grown 'inside out' from subsequent mergers, leading to the local size-mass relation (van Dokkum et al. 2015). However, massive galaxy merger theory relies on systems to self-regulate star formation through outflowing gas and dust, called feedback.

Despite the critical importance of feedback to the theorized evolutionary process, the physical mechanisms responsible for feedback remain poorly understood. Numerous potential sources of feedback are actively being studied, including active galactic nuclei (AGN) feedback, supernovae ram pressure, radiation pressure, shocks, and starbursts (e.g., Ceverino & Klypin 2009). The feedback from massive stars and supernovae is less efficient in massive galaxies, leading to the acceptance of AGN feedback as the primary driver of large-scale outflows (e.g., Rupke & Veilleux 2011, Cicone et al. 2014, Genzel et al. 2014). However, even with significant research efforts to confirm this scenario, it is still unclear if the strong ejective feedback required to quench star formation is powered by stars or AGN (e.g., Gabor & Bournaud 2014, Kocevski et

al. 2017), especially in compact galaxies. It is difficult to study the feedback mechanisms within compact massive galaxies at $z > 1.5$ due to their high redshifts. Fortunately, galactic outflows exist across multiple redshifts (e.g., Shapley et al. 2003, Weiner et al. 2009, Chen et al. 2010, Martin et al. 2012).

With the goal of understanding how the physical processes behind extreme outflows contribute to quenching star formation in massive galaxies, we began by selecting $z = 0.4 – 0.8$ galaxies from the Sloan Digital Sky Survey (SDSS) Data Release 7 that showed signs of very recent quenching. We required the galaxies to have young stellar populations dominated by A- and B-stars, but weak or absent nebular emission lines which indicate minimal ongoing star formation. We chose galaxies at $z > 0.4$ so that the Mg II λλ 2796,2803 Å doublet would be accessible in the optical range. Only galaxies with stellar masses of $\log(M_{\odot}) > 10.5$ were bright enough at $z > 0.4$ to be targeted by SDSS. These selection criteria yielded a total sample of 1089 galaxies, which were narrowed down to 49 galaxies that displayed recent quenching via blue B-star-dominated spectra. Tremonti et al. (2007) found 10 of these galaxies showed large Mg II outflow velocities (500 – 2000 km s^{-1}), which are much higher velocities than those typically exhibited by star-forming galaxies (300 km s^{-1}). Further follow-up on the reduced sample of 49 galaxies has revealed outflow velocities up to 3000 km s^{-1}. These large outflows are estimated to reach distances of ~100 kpc (Tremonti et al. 2007), which is consistent with sizes of outflows in high redshift ($z = 2 – 3$) galaxies (e.g., Steidel et al. 1996, Pettini et al. 2000, Pettini et al. 2001, Ceverino & Klypin 2009, Weiner et al. 2009, Steidel et al. 2010).

Although the targets were specifically post-starburst galaxies, Diamond-Stanic et al. (2012) found that many of the reduced sample were also detected by the Wide-field Infrared Survey Explorer (WISE) at 22 μm. The calculated obscured star formation rates (SFRs) indicated

surprisingly substantial (50 $M_{\odot}$ yr^{-1}) ongoing star formation within these galaxies (Diamond-Stanic et al. 2012), which seems to contradict their very blue optical and UV spectra. We have hypothesized that the galaxies are quenching outside-in, where star formation has ceased in the outer shell after the gas and dust has been blown out, leaving a dense, dusty star-forming core remaining.

Optical imaging using the Hubble Telescope (HST) of 29 galaxies with the youngest derived post-starburst ages ($t_{burst} \leq 300$ Myr) revealed very diverse galaxy morphologies (Sell et al. 2014). Two critical features present in all of the observed morphologies are tidal features indicative of recent mergers, as well as central unresolved compact cores ($r_e \sim 100$ pc). Sell et al. (2014) used the HST optical spectra, Chandra X-ray data, and near-Infrared colors to show that the dusty cores likely contain compact starbursts, with little to no AGN contribution. Furthermore, this concentrated, compact starburst indicates extremely high SFR surface densities (i.e. ~ 3000 $M_{\odot}$ yr^{-1} kpc^{-2}) approaching the Eddington limit for radiation pressure-driven feedback (Diamond-Stanic et al. 2012). It is entirely possible that starbursts from super compact nuclei can produce high velocity winds from massive stars and supernovae within (Heckman et al. 2011, Diamond-Stanic et al. 2012, Sell et al. 2014). Our studies thus far have led to a sample of galaxies at intermediate redshift that are super compact ($r_e \sim 100$ pc), incredibly massive ($M \geq 10^{11}$ $M_{\odot}$), bright blue late-stage and post-merging galaxies with some of the highest outflow velocities and SFR surface densities (Σ_{SFR}) among galaxies at any redshift (Tremonti et al. 2007, Diamond-Stanic et al. 2012, Geach et al. 2013, Geach et al. 2014, Sell et al. 2014). The extremity of the SFR surface densities and outflow velocities suggest these galaxies are in a brief but critical last stage of rapid quenching to assemble massive stellar bulges (Diamond-Stanic et al.

2012, Geach et al. 2013, Geach et al. 2014). By investigating this sample of unique galaxies, the similarities between them and other compact star-forming galaxies at higher redshifts will give us crucial insights into the formation of those high redshift galaxies that are difficult to directly observe.

For this project, we have obtained follow-up spectra from Keck/NIRSPEC on 14 of these galaxies in order to obtain high signal-to-noise (S/N) near-Infrared data. Our goal is to determine if the outflows are driven entirely by stellar feedback by learning all we can from the outflows in emission, as well as to understand the physical properties of the starburst in the dusty core. NIRSPEC covers Hα λ 6563 Å, [N II] λλ 6549,6584 Å, and [S II] λλ 6717,6731 Å, which are emission lines that can be used to examine gas ionization, star formation, and metallicity. These emission lines, with the addition of [O II] λλ 3726,3729 Å, Hβ λ 4861 Å, and [O III] λλ 4959,5007 Å from SDSS and the Multiple Mirror Telescope (MMT), will help us determine how the gas is ionized. We focus on 13/14 galaxies for this particular study as the omitted source was completely AGN-dominated.

In Section 2, we describe the observations and data reduction techniques used, with a brief explanation of the existing data already in hand (Sections 2.2 and Table 1). We then describe the fitting procedure for the NIRSPEC emission lines in Section 3, followed by a discussion of the results in Section 4.

2. OBSERVATIONS AND DATA REDUCTION

The 13 galaxies in this study were selected by the presence of spectra from the MMT. We describe the observation and reduction methods used to obtain these data. Section 2.1 outlines

our main data set from Keck/NIRSPEC. Our second data set is from combined SDSS and MMT spectra, described briefly in Section 2.2. The additional auxiliary data from our collaboration is shown in Table 1.

2.1 NIRSPEC

Data were taken using the Near Infrared Spectrometer (NIRSPEC) on Keck II. Observing dates were September 15th-17th, 2013 and January 16th-17th, 2014. The target wavelength range was λ_{rest} = 6500-6800 Å in order to observe Hα, [N II], and [S II]. All exposures used the 24x0.760 arcsecond slit. NIRSPEC resolution is 12 km s^{-1}. For each object, a series of 300 second exposures were taken at two different positions along the slit. The subtraction of these two positions allowed for the elimination of sky lines and dark currents. All objects were observed for 40-60 minutes in total, but some exposures were not included due to alignment and guiding issues, clouds, and moon interference.

The REDSPEC IDL package was used to make spatial (spatmap) and spectral (specmap) corrections to the raw data. Calibrator stars were observed at two different positions along the slit, just like each object. For each position and filter, calibrator star spectra were averaged together to create master spectra for each position, which could then be used for the corresponding raw target exposures. The effective temperature was set based on the spectral type of the calibrator star. Calling spatmap on the two positions of the calibrator star in a given filter allowed for curvature correction in the wavelength-space plane. Then specmap allowed stellar lines to be matched with known wavelengths by doing a series of fits in increasing order until you have a fit of third order with residuals < 0.1.

Using REDSPEC, stellar lines are removed to leave a smooth blackbody spectrum. The same procedure is used for the targets to produce spectra that are ready for flux calibration and

data analysis. Following the pipeline produces 2-6 analysis-ready spectra per object. These produced spectra were averaged to produce a single final spectrum for each galaxy, and the standard deviation was used to create a final error spectrum. Furthermore, NIRSPEC spectra were adjusted to match the flux of the extended continuum from the MMT/SDSS data single stellar population (SSP) fits (see Section 2.2). All spectra were converted to vacuum wavelengths and corrected for heliocentricity.

Table 1
Source Information

ID	z	RA (J2000)	Dec. (J2000)	$\log(M_*/M_\odot)$	r_e (kpc)	SFR ($M_\odot$ yr^{-1})	Σ_{SFR} ($M_\odot$ yr^{-1} kpc^{-2})	MgII Velocity km s^{-1}
(1)	(2)	(3)	(4)	(5)	(6)	(7)	(8)	(9)
J0106-1023	0.4546	16.601056	-10.391647	11.3883		120		-1527
J0826+4305	0.6025	126.66006	43.091498	11.2490	0.214	287	517.964	-1228
J0901+0314	0.4586	135.38926	3.2367997	11.5977		119		-1206
J0905+5759	0.7114	136.34832	57.986791	11.2696	0.100	339	6026.37	-2470
J0944+0930	0.5127	146.07437	9.5053855	11.1481	0.133	184	1184.22	-1778
J1107+0417	0.4666	166.76197	4.2840984	11.0063		183		-1828
J1125-0145	0.5189	171.32874	-1.7590066	11.4051		119		-2011
J1341-0321	0.6612	205.40333	-3.3570199	10.8927	0.100	515	6159.07	-875
J1506+5402	0.6071	226.65124	54.039095	11.6190	0.165	683	698.319	-1211
J1613+2834	0.4502	243.38552	28.570772	11.4324	0.980	429	40.6833	-2416
J1713+2817	0.5765	258.25161	28.285631	11.1138	0.173	32	457.354	-868
J2116-0624	0.7279	319.10479	-6.5791139	11.1925		149		-1456
J2118+0017	0.4592	319.60026	0.29150705	11.6443	2.240	233	1.92069	0

Notes:
(5) Median stellar mass from iSED fitting.
(6) Effective radii from HST.
(7) SFRs from WISE observations.
(8) SFR surface densities calculated from (6) and (7).
(9) MgII $\lambda\lambda$2796,2803 Å absorption velocities.

2.2 SDSS and MMT

The original sample was selected from SDSS Data Release 7 (Adelman-McCarthy et al. 2006). Additionally, Tremonti et al. (2007) obtained higher S/N spectra of our targets using the Blue Channel Spectrograph on the 6.5 m MMT. They had spectral coverage from 4050 Å to 7200 Å with a dispersion of 1.19 Å per pixel using the 500 lines per mm grating blazed at 5600 Å. For the galaxies within z = 0.51 – 0.75, this yielded rest frame coverage of 2700 – 4100 Å.

These spectra were patched together with spectra from SDSS between 4500 and 4700 Å with a resolution range of 73 – 182 km s^{-1}. The final combined MMT/SDSS spectra can be seen

in Figure 1, including continuum fits and coverage of Mg II absorption features (v = 1000 – 2500 km s^{-1}). Our sources have strong post-starburst components (~10 Myr) with more recent, very blue starbursts (~1-3 Myr). Multiple episodes of star formation are consistent with late-stage mergers that are 2-3 passes from coalescence. The relative strengths of these starburst features vary, but most of our sources have strong Balmer absorption.

3. EMISSION LINE FITTING

In this section, we describe the procedures for fitting Hα, [N II], and [S II] from NIRSPEC, as well as [O II], Hβ, and [O III] from MMT/SDSS. These two data sets were not fit simultaneously due to differences in resolutions and some kinematics, so the higher S/N NIRSPEC data was used for initial fit parameters for MMT/SDSS. However, most sources exhibited similar kinematics, allowing us to justify using the separate fitting approach without forcing extra constraints. Additionally, [O II] was fit separately from Hβ and [O III] because [O II] shows different behavior in most cases.

MPFITFUN in IDL was used to fit 1-2 Gaussian profiles per emission line. NIRSPEC spectra were continuum-subtracted using the extended SSP continuum fits. Given the low S/N of some of the spectra, a simple linear power law was fit to further constrain the continuum levels. Sources with potential broad components were first fitted with one broad line for the blended Hα-[N II] region to find an upper limit for the broad Hα flux, and then fit again with three separate broad components. In order to set some constraints to separate the blended lines, the broad [N II] ratio was fixed to be the same as the narrow [N II] ratio. However, the [N II] lines were not fixed to be 1:3, but instead allowed to be free due to the blue [N II] λ 6548 line being near the edge of the bandwidth, where the noise is inherently worse. Narrow and broad full

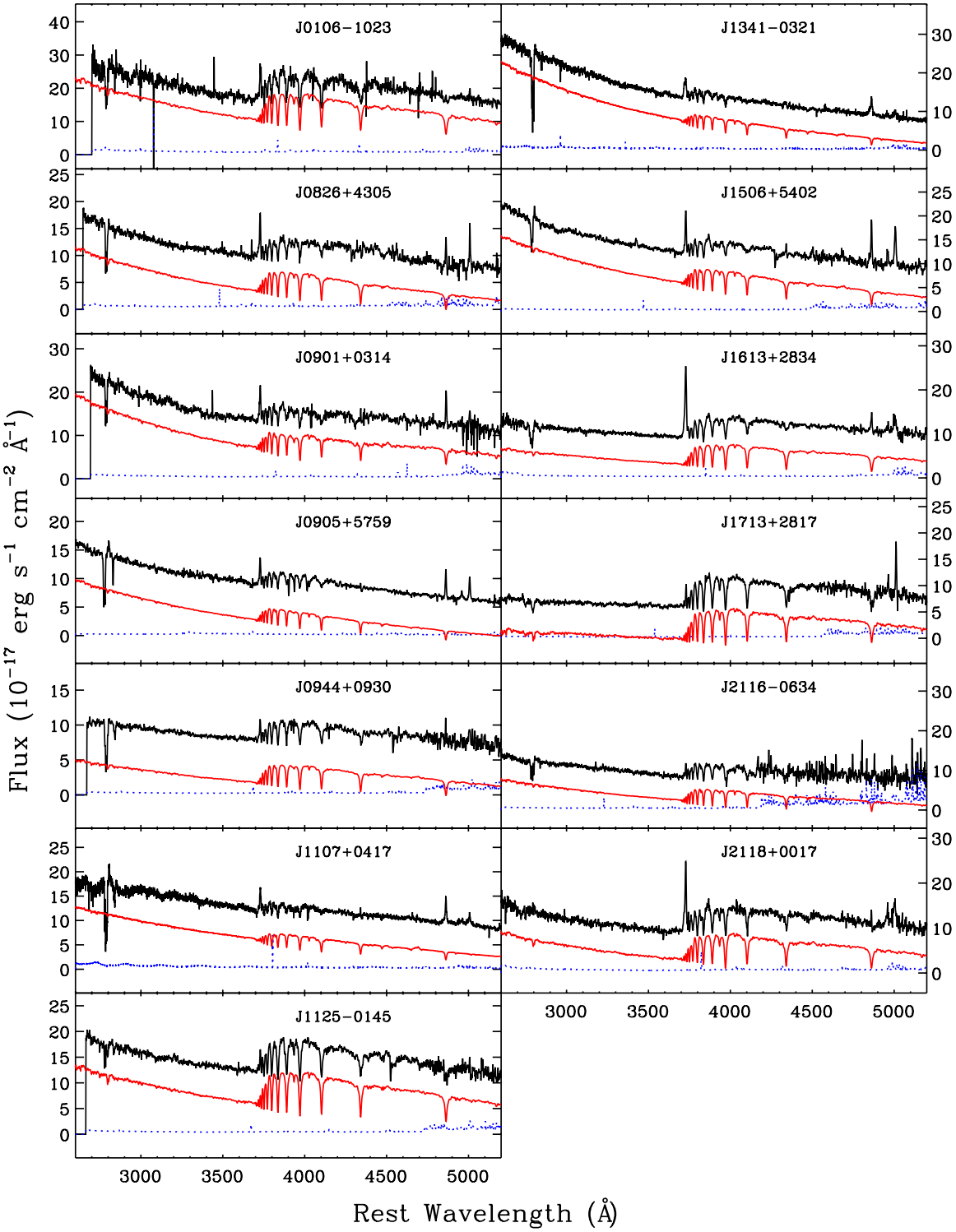

Figure 1. The combined MMT and SDSS rest-frame optical spectra, shown above in black, patched together between 4500 and 4700 Å. The best fit to each continuum is shown in red, offset vertically for clarity, with the error spectra shown in blue. In general, the spectra are very blue and exhibit strong Balmer absorption features, similar to spectra of post-starburst galaxies, but also a blue component from the most recent starburst period.

widths at half maximum (FWHMs) were fixed to be self-consistent for each source, where narrow lines were given a starting sigma of 3-5 and broad were given starting values of 6-20 sigma. In general, there was not high enough S/N to also fit broad [S II] components, except for in J1506, J1613, and J2118.

From there, the MMT/SDSS spectra were continuum-subtracted and fit with a simple linear power law. The MMT/SDSS spectra were then given initial conditions similar to those used for NIRSPEC fits. First, Gaussians were fit to each narrow emission line for Hβ and [O III]. For those with broad features, an additional Gaussian was fit to each. The broad Hβ centroid was allowed to be free, except in some cases where it was obvious the broad component was not redshifted and therefore was forced to be blueshifted. [O III] line centroids and FWHMs were tied to those of Hβ for both broad and narrow lines respectively. Additionally, both the broad and narrow [O III] lines were forced to have a flux ratio of 1:3 to aid in fitting the lower S/N [O III] λ 4959 Å line. FWHMs from MMT/SDSS fits were deconvolved using the average resolution of a small region around Hβ. This process was then repeated for the [O II] doublet, which lacked the resolution to distinguish between the two heavily blended lines, so the flux ratio was fixed to be 1:3.5.

Although these sources are already a unique sample, we had a few sources with unusual features that had to be handled differently. The first of these was J0905 in that it had no usable [S II] data but also had an offset red Hα component. This offset feature was fit separately with a narrow line because no broad fit was able to correctly account for its presence (see Figure 2). This offset component was then excluded from further analysis, but with the low S/N of the spectra, there could be a possible offset [N II] component.

Figure 2. The MMT/SDSS and NIRSPEC spectra of relevant emission line features. The first column shows the [O II] λλ 3726,3729 Å doublet from MMT. The second shows Hβ λ 4861 Å. The third column shows [O III] λλ 4959,5007 Å. The blended Hα λ 6563 Å and [N II] λλ 6548,6583 Å feature is in the fourth column, and the fifth column has the [S II] λλ 6717,6731 Å doublet. The error spectra are plotted in green dots, with fits shown in different colors: light blue shows the narrow line fits, pink shows the broad fits, and purple shows the total fit. Spectra are omitted where there was too much noise to observe any conclusive emission. KCWI data allowed us to fit broad components to [S II] for J2118, while J1506 and J1613 were the only other galaxies with high enough S/N to fit broad [S II] components. J0826 has by far the most blue-shifted broad [O II]. Upon closer inspection, this broad component has a S/N of 6.5, suggesting it is real. In most other cases, we desire stronger S/N to make confident conclusions.

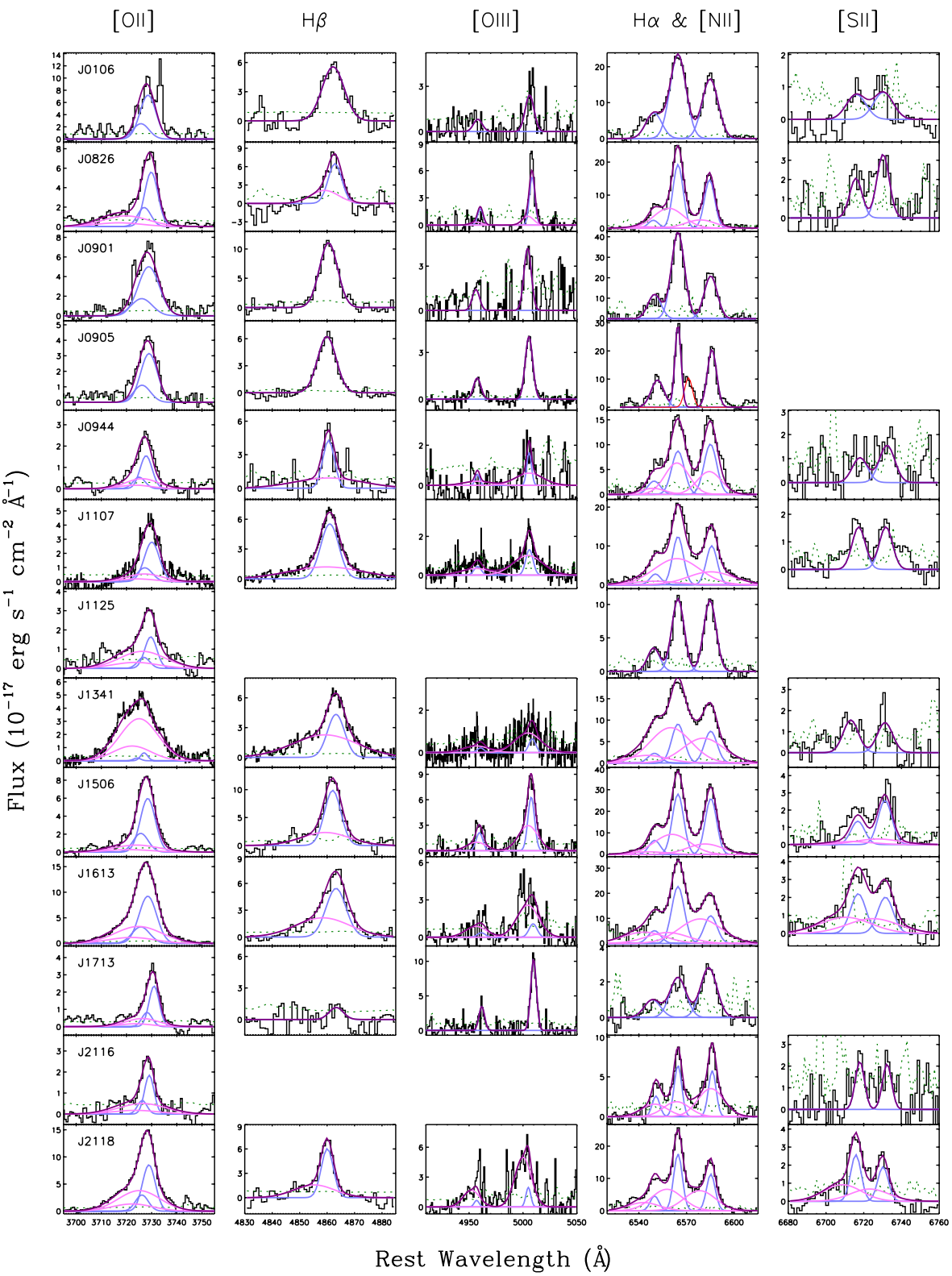
[OII]
Hβ
[OIII]
Hα & [NII]
[SII]
J0106
J0826
J0901
J0905
J0944
J1107
J1125
J1341
J1506
J1613
J1713
J2116
J2118
Flux (10^-17 erg s^-1 cm^-2 Å^-1)
Rest Wavelength (Å)

J1341 was odd in the fact that it exhibited the most significant broad components of the entire sample. Additionally, the [S II] portion of its spectra had an absorption feature, which was excluded from analysis.

Table 2
Fit Information

ID	NIRSPEC Narrow FWHM (km s^{-1})	NIRSPEC Broad FWHM (km s^{-1})	NIRSPEC v_{off} (km s^{-1})	MMT/SDSS Narrow FWHM (km s^{-1})	MMT/SDSS Broad FWHM (km s^{-1})	MMT/SDSS v_{off} (km s^{-1})
(1)	(2)	(3)	(4)	(5)	(6)	(7)
J0106-1023	541 (6)			566 (43)		
J0826+4305	345 (11)	1006 (118)	-263 (73)	326 (0)	724 (180)	-232 (113)
J0901+0314	440 (10)			446 (21)		
J0905+5759	203† (21)			469 (6)		
J0944+0930	426 (0)	814 (257)	-32 (126)	278 (52)	1801 (578)	4 (21)
J1107+0417	484 (0)	1979 (0)	-45 (5)	473 (14)	1965 (97)	-80 (35)
J1125-0145	416 (14)			345 (60)		
J1341-0321	425 (29)	1379 (102)	-211 (45)	444 (20)	1710 (65)	-247 (28)
J1506+5402	384 (7)	1209 (60)	-170 (24)	416 (35)	1268 (163)	-167 (70)
J1613+2834	428 (24)	1413 (92)	-299 (8)	506 (46)	1425 (123)	-297 (83)
J1713+2817	551 (25)			350 (24)		
J2116-0624	255 (38)	876 (183)	-40 (79)			
J2118+0017	292 (16)	1060 (40)	-245 (37)	289 (16)	1072 (40)	-294 (45)

† J0905 has an unusual Hα and [NII] feature where all three lines were not tied together using the Hα FWHM.
(2)-(4): FWHMs and velocity offsets of broad features based on Hα from the NIRSPEC spectra.
(5)-(7): FWHMs and broad velocity offsets based on Hβ from MMT.

The final unique source was J2118, which was fit using constraints from Keck/KCWI observations completed by Rupke et al. (2019). The continuum-subtracted MMT/SDSS spectrum for J2118 was fit to have the Hβ centroid and FWHM to be within 0.1% of the KCWI results. The [O III] lines were then tied to Hβ during the fitting process. For the continuum-subtracted J2118 NIRSPEC data, Hα was constrained to have its centroid and FWHM to be within 1% of the KCWI data, with [N II] and [S II] being tied to Hα during fitting. Because KCWI has much higher S/N than MMT, SDSS, and NIRSPEC, we were able to fit significant broad components to the [S II] doublet (see Figure 2).

4. RESULTS AND DISCUSSION

For Figure 2, fits were done separately for the two sets of spectra since fitting simultaneously did not improve the quality of the fits. 8/13 of our sources have distinguishable broad emission components across most of the emission lines examined here. Additionally, [O II] has different kinematics in some cases, furthering our argument to fit the groups of lines separately. In fact, almost all of the galaxies exhibit significant broad [O II] components. This doublet is extremely blended, so the ratio of the two lines was fixed. Usually [O II] is a good proxy for the electron density, but the doublet is almost indistinguishable from a single line in our spectra. We instead use [S II] to estimate electron density (see Figure 3). Even though it has low S/N, the [S II] doublet is distinguishable enough to calculate its ratio, giving us a more reliable electron density. However, the broad [N II] and [S II] ratios were fixed to be the same as the narrow ratios. This helped us with deblending the [N II]-Hα feature and tackling the low S/N for the three sources we were able to fit broad [S II]. Using the method from Sanders et al. (2016), the inverse variance weighted average electron density for these sources is 121 cm^{-3}, whereas the ordinary average is 1465 cm^{-3}. The median electron density is 505 cm^{-3}, which is a factor of two higher than the star-forming regions at $z \sim 2$ studied by Sanders et al. (2016), which makes sense given the incredibly compact nature of our sources.

Normally when broad components are present in hydrogen lines, it is indicative of an AGN, but we also see broad lines in [O III] and [N II]. The Mg II emission also is not broad like that of a quasar, which alone can suggest no AGN presence. Therefore, we did not make the

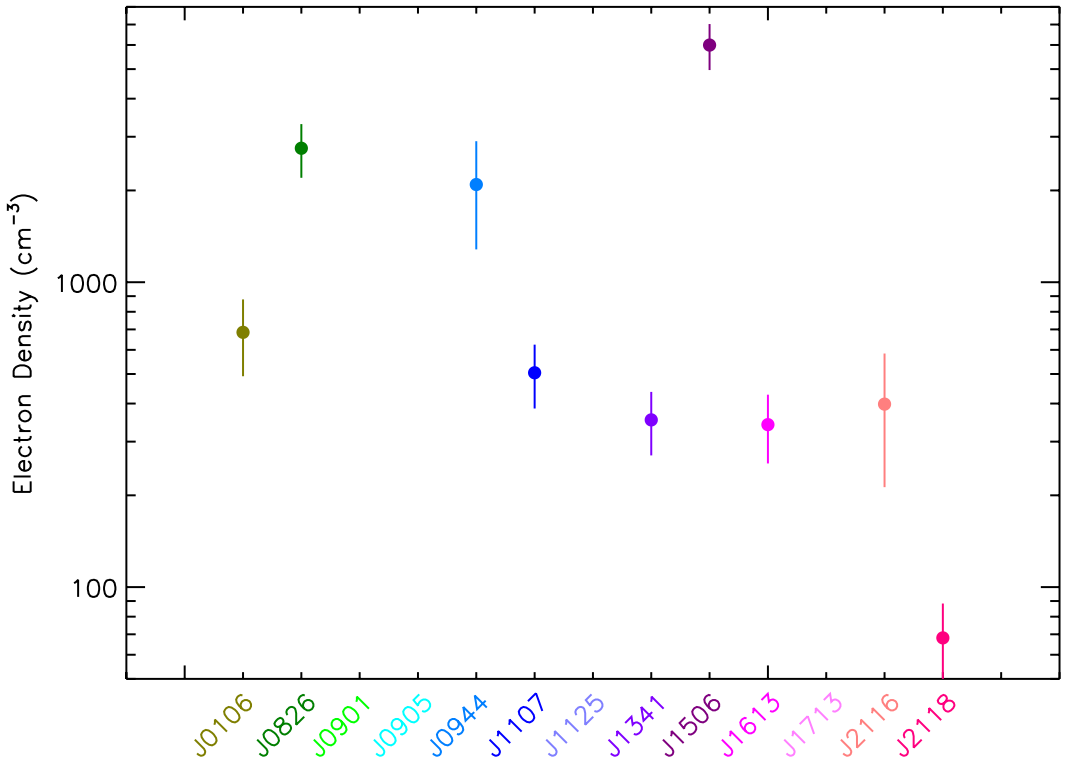

Figure 3. Electron densities calculated from the method described by Sanders et al. (2016) using narrow [S II] doublet ratio from our NIRSPEC data. Data is omitted where fits were inconclusive. All of the [S II] doublet ratios come from the narrow flux measurements. In order to fit the lower S/N lines with broad, the three sources with broad fits were fixed to have the same doublet ratio in broad as in narrow. Errors shown are percent errors from the [S II] doublet ratio.

assumption that AGN are present. Our first step was to make a BPT (Baldwin, Philips, & Terlevich 1981) diagram using total flux (see Figure 4) in addition to classic narrow-only flux. The advantage of [O III]/Hβ, [N II]/Hα, and [S II]/Hα is that these ratios are close in wavelength so are mostly independent from reddening. Sources that are beneath the Kauffman et al. (2003) empirical line are sources ionized by hot stars, while those that are above are considered to be ionized more powerful sources. Additionally, we used the SDSS Data Release 7 as our comparison sample. Cuts were made to ensure S/N of each emission line was ≥ 3, with the addition of a redshift cut of $0.005 < z < 0.25$.

[N II]/Hα shows most of our galaxies in the composite region, with the bulk shift happening more in [O III]/Hβ between narrow and total than in [N II]/Hα. The characteristics of these galaxies indicate that the starburst and possibly shocks are responsible for pushing these galaxies into the composite region rather than a heavily obscured AGN. The one exception to this is J1713, which can be seen clearly in Figure 4. J1713 has almost no Hβ (see Figure 2), which is a strong indicator of an AGN presence, as well as its low SFR (see Table 1). The lack of bulk movement upon exemption of broad emission only furthers our idea of these sources not being dominated by AGN. Instead, the presence of broad lines is most likely due to a combination of shocks and feedback from the compact starburst. Additionally, ionization potentials for [O III] are higher than for [N II] and [S II], and [O III] is too dense to come from the broad line region of an AGN. [O III] traces shocks, so it is most likely tracing the most ionized part of the multiphase outflows.

Examining the total flux shows these galaxies have diminished [S II]/Hα, which is unusual but could possibly indicate Lyman alpha leakage. The narrow [S II] ratio looks fairly normal. Only 3 sources had high enough S/N to see a broad component in [S II] so the shift of [S II]/Hα comes mostly from the presence of broad Hα. We lack sufficient S/N to make conclusive judgements about broad [S II] in the rest of our sample, but it would be strange to have broad components in other forbidden lines but not in [S II]. Therefore, the total flux comparisons shown in Figure 4 are more robust, and therefore potentially more trustworthy. [S II] is produced in the outermost layers of density-bounded H II regions, which seems to indicate that the H II regions in our sources are running out of gas before the ionizing photons are all absorbed.

When isolating the sources with broad emission, which can be seen in Figure 5, the broad ratios span all regions of the BPT, while the narrow stays within the composite region. This

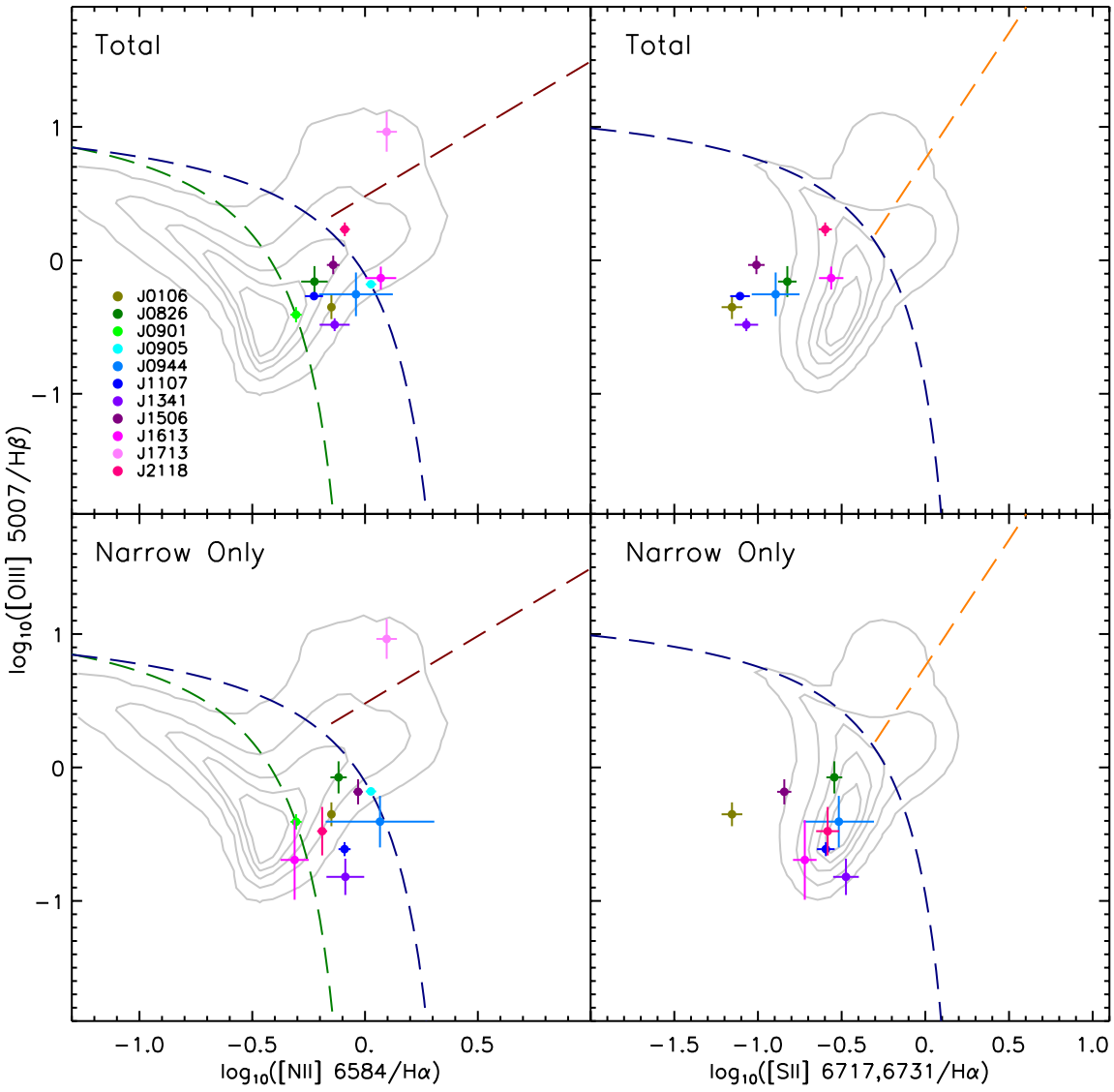

Figure 4. Here we show BPT diagrams for the traditional narrow flux ratios and also the total flux ratios. The green dashed line is the empirical separation of SFGs and AGN from Kauffman et al. (2003) for [N II]/Hα, and the blue dashed lines are from Kewley et al. (2001, 2006) which indicate the theoretical maximal starburst, above which galaxies are usually considered to be AGN-dominant. The red dashed line is the Liner-Seyfert separation for [N II]/Hα (Cid-Fernandes et al. 2010), and the orange dashed line denotes the separation between Liner and Seyfert galaxies for [S II]/Hα (Kewley et al. 2006). The light grey contours are galaxies from SDSS Data Release 7, with contour levels at 30%, 50%, 70%, 90%, and 99%. For both total and narrow flux ratios, our sample stays within the composite region, with the exception of J1713, which is a prime AGN candidate. The other main feature is the shift of [S II]/Hα by 0.5-1 dex between the total and narrow ratios, with some of our galaxies having a lower [S II] total ratio than 99% of SDSS galaxies. Although we may lack significant S/N to make any definitive conclusions for the cause of this shift, the [S II]/Hα ratio is diminished in total flux due to the presence of broad Hα more so than broad [S II].

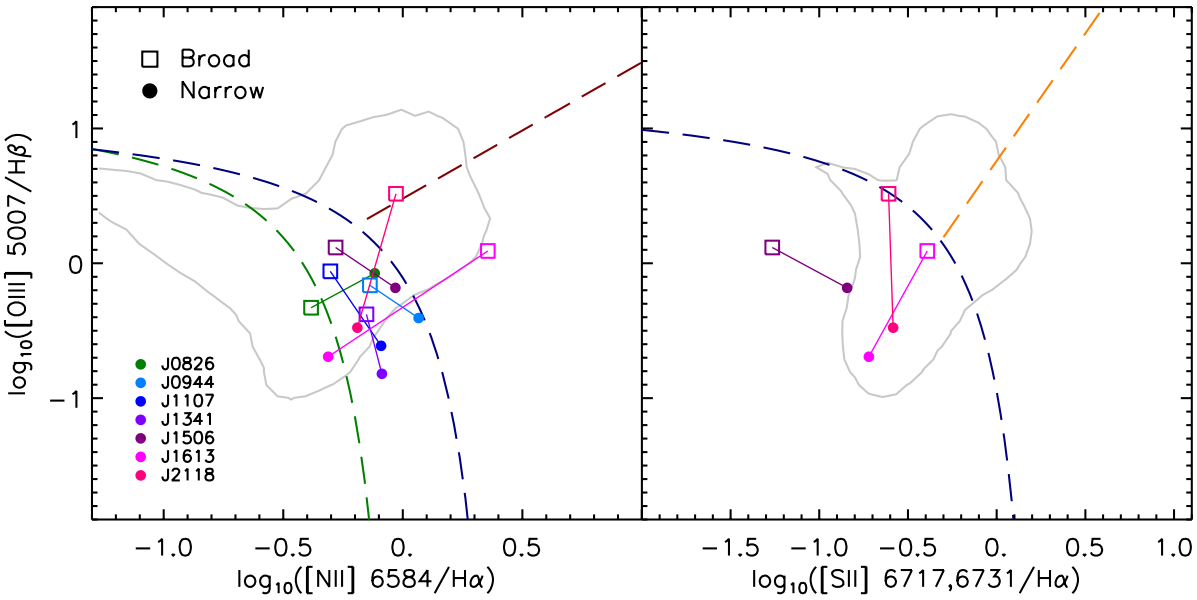

Figure 5. BPT diagrams for the broad components. Only three sources are shown for the [S II]/Hα panel where reliable fits could be made to broad components. All dashed lines are the same as described in Figure 4, with only the 99% SDSS DR7 contour shown in grey for clarity. There is no noticeable bulk shift between the narrow and broad components for either Hα ratio, however there is a systematic shift to higher [O III]/Hβ looking between narrow and broad.

scattered behavior further solidifies how [O III] is tracing the outflows in their different phases. Only J1613 and J2118 have broad components above the theoretical maximal starburst line, so they are the more likely in our sample to have an obscured AGN than the other broad sources.

Figure 6 shows how [N II]/[S II] compares to stellar mass, SFRs, and Σ_{SFR}. Additionally, our sources are also compared to that of our Sloan comparison sample. [N II]/[S II] is often used as an indicator of metallicity. For the first panel, our sources tend to have higher metallicity that the sources from SDSS, as well as being some of the most massive galaxies as we already know. The middle panel again clearly displays the higher metallicity, but also the how significant the obscured SFRs in our sources are. The last panel shows how exceptionally high our star formation rate surface densities are, which illustrates the extreme nature of these super compact, massive galaxies.

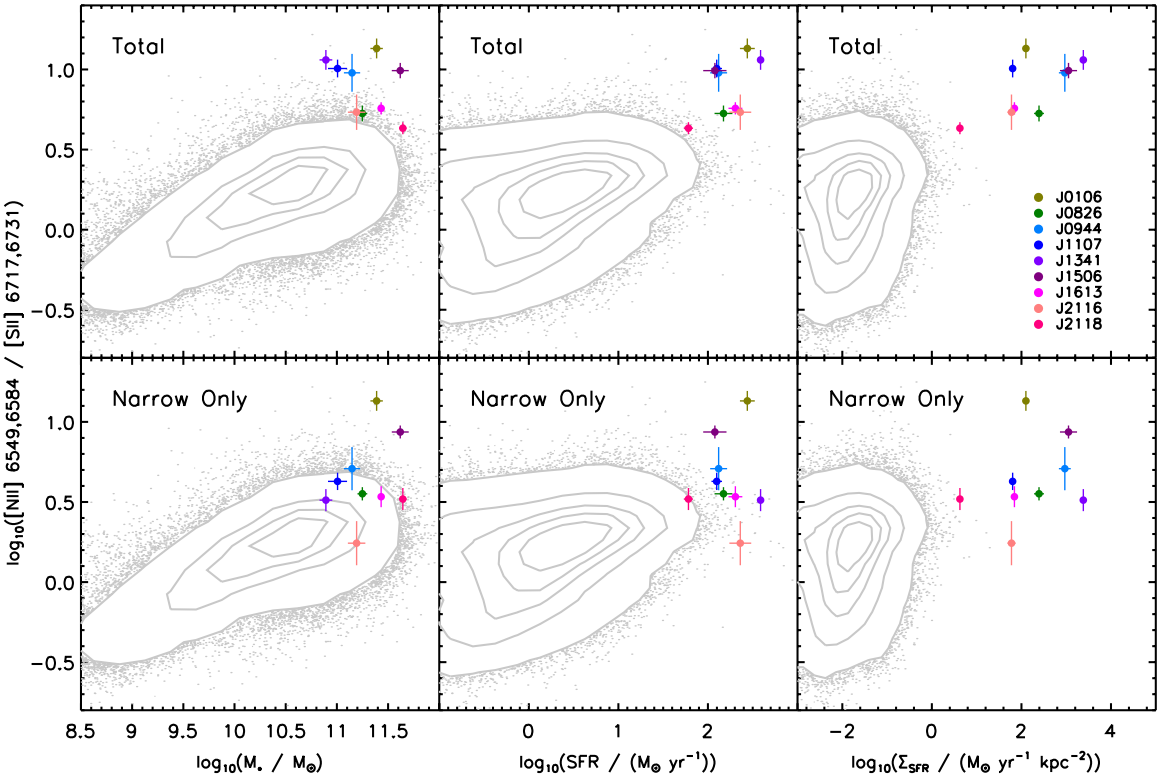

Figure 6. [N II]/[S II] compared to stellar mass, star formation rate, and star formation rate surface density. The grey contours represent SDSS DR7 data with contours at 25%, 50%, 75%, 90%, and 98%, with outliers plotted individually. The top row shows total flux for these emission lines, while the bottom row shows only the narrow components of the emission lines.

For Figure 7, the [O III] maximal outflow velocities are determined by method described in Rupke & Veilleux (2013). The Mg II absorption velocity is from Tremonti et al. (2007). It is also important to note that J2118 has no absorption velocity in Mg II and likely has Mg II emission, so Fe II is shown instead. Our galaxies are not spherically symmetric, but most likely bipolar (Sell et al. 2014; Rupke et al. 2019). This further throws into speculation the true physical sources of the broad component, especially considering projection effects. However, Figure 7 shows clearly that the absorption and the emission are both tracing similar outflowing gas, which tells us the outflows have multiple phases. We do not see much absorption at systemic, so it may be heavily obscured, especially given that absorption is seen only in your line

of sight. Emission is seen throughout the whole shell, so we can see both blueshifted and redshifted flux in emission.

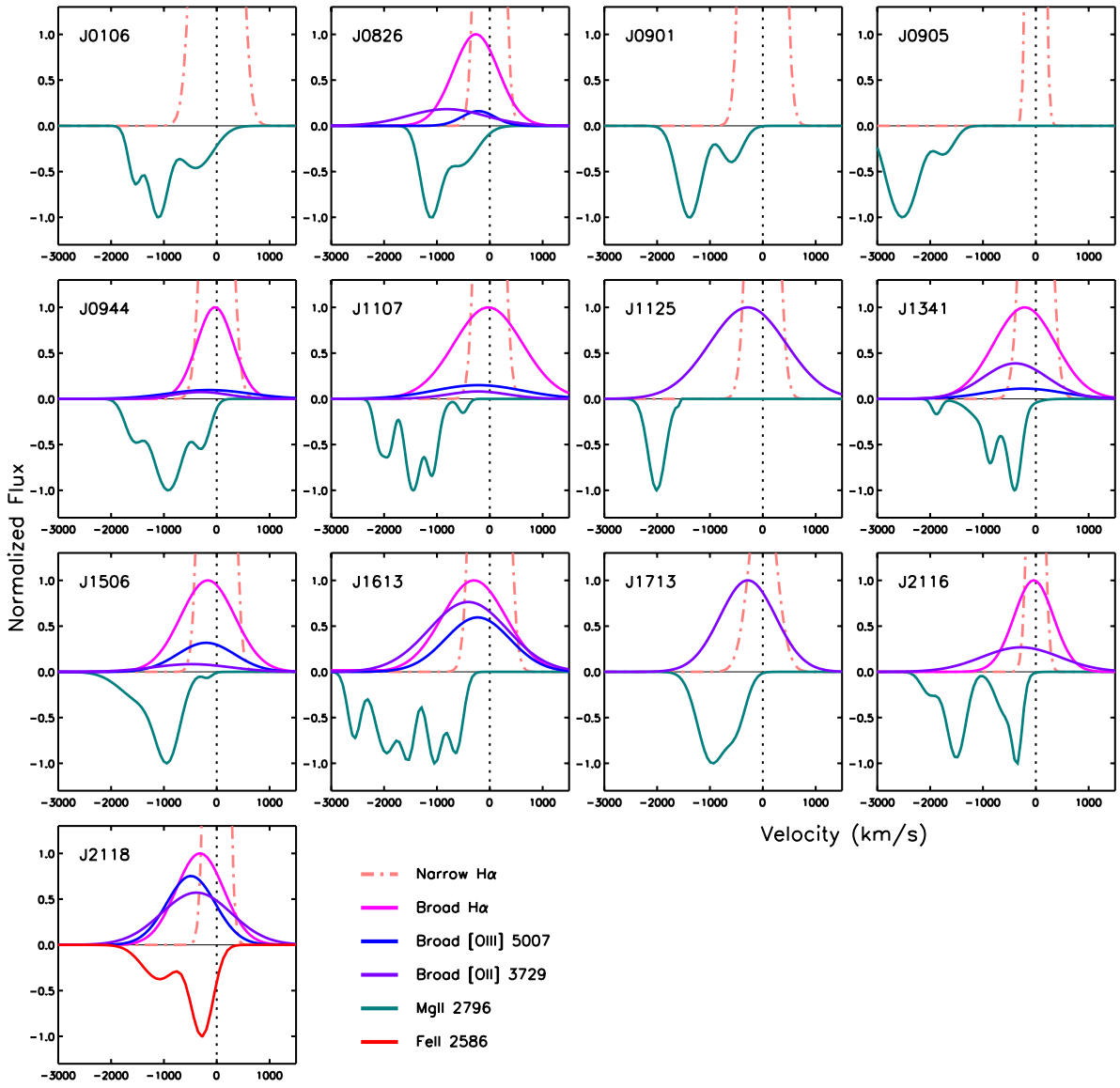

Figure 7. Fits to select broad emission lines as well as Mg II λ2796 absorption and narrow systemic Hα in velocity space. Many of these lines are part of a doublet, but here we chose to show single, decoupled lines. Most of the emission lines trace each other well, with the exception of [O II] λ3729 which tends to be further blueshifted with respect to systemic. Many of the broad lines have comparable velocities to the outflow indicated by Mg II, meaning the broad lines are part of the outflow. All emission line fluxes are normalized to that of broad Hα, which is set to 1. Both Mg II λ2796 and, in the case of J2118, Fe II λ2586, are normalized to -1 for an easier comparison. J2118 has Mg II emission, so we opted to show the Fe II absorption profile instead of Mg II.

5. CONCLUSIONS

From this work, we have seen how [O III] emission especially traces the outflowing ionized gas. We know that even though these galaxies appear very blue, they still contain substantial amounts of dust. This means that even though we would theoretically see all emission from a galaxy since it does not depend on the line of sight, the redshifted emission is most likely heavily obscured.

Any potential AGN feedback within these galaxies must then be highly obscured. Apart from J1713, which is the most likely candidate to host an AGN, no other galaxies displayed any definitive indications of the presence of an AGN. Given the extremely compact starbursts happening within, we have very strong evidence that the outflows in these sources are generated by the starbursts. The high velocities of these outflows reflect the extreme power behind them of the near Eddington-limited surface densities.

The insights gained from this thesis have opened up further avenues to explore, especially with adding more galaxies from the parent sample. The diverse morphologies of our sources include unusual dust extinction profiles that must be analyzed further. The depleted [S II] content of these galaxies could suggest Lyman alpha leakage, which is a relatively new area of research. Additionally, with newer data, we will be able to estimate mass loading factors and other physical properties of the outflows and explore how the outflows are related to the various merger stages in our sample.

Both Dr. Coil and Dr. Perrotta are co-authoring a publication with the thesis author in preparation to be submitted later this year. This includes all sections and some of the figures, but with the acquisition of higher quality data that is not present in this thesis.

6. REFERENCES

Alexandroff, R. M., Heckman, T. M., Borthakur, S., Overzier, R., & Leitherer, C. 2015, ApJ, 810, 104

Arribas, S., Colina, L., Bellocchi, E., Maiolino, R., & Villar-Martín, M. 2014, A&A, 568, A14

Barro, G., Faber, S. M., Pérez-González, P. G., Koo, D. C., Williams, C. C., Kocevski, D. D., Trump, J. R., Mozena, M., McGrath, E., van der Wel, A., Wuyts, S., Bell, E. F., Croton, D. J., Ceverino, D., Dekel, A., Ashby, M. L. N., Cheung, E., Ferguson, H. C., Fontana, A., Fang, J., Giavalisco, M., Grogin, N. A., Guo, Y., Hathi, N. P., Hopkins, P. F., Huang, K.-H., Koekemoer, A. M., Kartaltepe, J. S., Lee, K.-S., Newman, J. A., Porter, L. A., Primack, J. R., Ryan, R. E., Rosario, D., Somerville, R. S., Salvato, M., & Hsu, L.-T. 2013, ApJ, 765, 104

Baldwin, J. A., Phillips, M. M., & Terlevich, R. 1981, ASP, 93, 5

Ceverino, D. & Klypin, A. 2009, ApJ, 695, 292

Chen, Y.-M., Tremonti, C. A., Heckman, T. M., Kauffmann, G., Weiner, B. J., Brinchmann, J., & Wang, J. 2010, AJ, 140, 445

Cicone, C., Maiolino, R., Sturm, E., Graciá-Carpio, J., Feruglio, C., Neri, R., Aalto, S., Davies, R., Fiore, F., Fischer, J., García-Burillo, S., González-Alfonso, E., Hailey-Dunsheath, S., Piconcelli, E., & Veilleux, S. 2014, A&A, 562, A21

Cid Fernandes, R., Stasinska, G., Schlickmann, M. S., Mateus, A., Vale Asari, N., Schoenell, W., & Sodré, L., Jr. 2010, MNRAS, 403, 1036

Davies, R. L., Förster Schreiber, N. M., Übler, H., Genzel, R., Lutz, D., Renzini, A., Tacchella, S., Tacconi, L. J., Belli, S., Burkert, A., Carollo, C. M., Davies, R. I., Herrera-Camus, R., Lilly, S. J., Mancini, C., Naab, T., Nelson, E. J., Price, S. H., Shimizu, T. T., Sternberg, A., Wisnioski, E., & Wuyts, S. 2019, ApJ, 873, 122

Diamond-Stanic, A. M., Moustakas, J., Tremonti, C. A., Coil, A. L., Hickox, R. C., Robaina, A. R., Rudnick, G. H., & Sell, P. H. 2012, ApJ, 755, L26

Dopita, M. A., Kewley, L. J., Sutherland, R. S., & Nicholls, D. C. 2016, ASS, 361, 61

Förster Schreiber, N. M., Genzel, R., Newman, S. F., Kurk, J. D., Lutz, D., Tacconi, L. J., Wuyts, S., Bandara, K., Burkert, A., Buschkamp, P., Carollo, C. M., Cresci, G., Daddi, E., Davies, R., Eisenhauer, F., Hicks, E. K. S., Lang, P., Lilly, S. J., Mainieri, V., Mancini, C., Naab, T., Peng, Y., Renzini, A., Rosario, D., Shapiro Griffin, K., Shapley, A. E., Sternberg, A., Tacchella, S., Vergani, D., Wisnioski, E., Wuyts, E., & Zamorani, G. 2014, ApJ, 787, 38

Freeman, W. R., Siana, B., Kriek, M., Shapley, A. E., Reddy, N., Coil, A. L., Mobasher, B., Muratov, A. L., Azadi, M., Leung, G., Sanders, R., Shivaei, I., Price, S. H., DeGroot, L., & Kereš, D. 2019, ApJ, 873, 102

Gabor, J. M. & Bournaud, F. 2014, MNRAS, 441, 1615

Geach, J. E., Hickox, R. C., Diamond-Stanic, A. M., Krips, M., Moustakas, J., Tremonti, C. A., Coil, A. L., Sell, P. H., & Rudnick, G. H. 2013, ApJL, 767, L17

Geach, J. E., Hickox, R. C., Diamond-Stanic, A. M., Krips, M., Rudnick, G. H., Tremonti, C. A., Sell, P. H., Coil, A. L., & Moustakas, J. 2014, Nature, 516, 68

Genzel, R., Förster Schreiber, N. M., Rosario, D., Lang, P., Lutz, D., Wisnioski, E., Wuyts, E., Wuyts, S., Bandara, K., Bender, R., Berta, S., Kurk, J., Mendel, J. T., Tacconi, L. J., Wilman, D., Beifiori, A., Brammer, G., Burkert, A., Buschkamp, P., Chan, J., Carollo, C. M., Davies, R., Eisenhauer, F., Fabricius, M., Fossati, M., Kriek, M., Kulkarni, S., Lilly, S. J., Mancini, C., Momcheva, I., Naab, T., Nelson, E. J., Renzini, A., Saglia, R., Sharples, R. M., Sternberg, A., Tacchella, S., & van Dokkum, P. 2014, ApJ, 796, 7

Hayward, C. C. & Hopkins, P. F. 2017, MNRAS, 465, 1682

Heckman, T. M., Borthakur, S., Overzier, R., Kauffmann, G., Basu-Zych, A., Leitherer, C., Sembach, K., Martin, D. C., Rich, R. M., Schiminovich, D., & Siebert, M. 2011, ApJ, 730, 5

Ho, I-T., Kewley, L. J., Dopita, M. A., Medling, A. M., Allen, J. T., Bland-Hawthorn, J., Bloom, J. V., Bryant, J. J., Croom, S. M., Fogarty, L. M. R., Goodwin, M., Green, A. W., Konstantopoulos, I. S., Lawrence, J. S., López-Sánchez, Á. R., Owers, M. S., Richards, S., & Sharp, R. 2014, MNRAS, 444, 3894

Ho, I-T., Kudritzki, R.-P., Kewley, L. J., Jabran Zahid, H., Dopita, M. A., Bresolin, F., & Rupke, D. S. N. 2015, MNRAS 448, 2030

Ho, I-T., Medling, A. M., Bland-Hawthorn, J., Groves, B., Kewley, L. J., Kobayashi, C., Dopita, M. A., Leslie, S. K., Sharp, R., Allen, J. T., Bourne, N., Bryant, J. J., Cortese, L., Croom, S. M., Dunne, L., Fogarty, L. M. R., Goodwin, M., Green, A. W., Konstantopoulos, I. S., Lawrence, J. S., Lorente, N. P. F., Owers, M. S., Richards, S., Sweet, S. M., Tescari, E., & Valiante, E. 2016, MNRAS, 457, 1257

Kauffmann, G., Heckman, T. M., Tremonti, C., Brinchmann, J., Charlot, S., White, S. D. M., Ridgway, S. E., Brinkmann, J., Fukugita, M., Hall, P. B., Ivezic, Z., Richards, G. T., & Schneider, D. P. 2003, MNRAS, 346, 1055

Kennicutt, R. C., Jr. 1998, ARAA, 36, 189

Kewley, L. J., Dopita, M. A., Sutherland, R. S., Heisler, C. A., & Trevena, J. 2001, ApJ, 556, 121

Kewley, L. J., Groves, B., Kauffmann, G., & Heckman, T. 2006, MNRAS, 372, 961

Kewley, L. J., Dopita, M. A., Leitherer, C., Davé, R., Yuan, T., Allen, M., Groves, B., & Sutherland, R. 2013, ApJ, 774, 100

Kocevski, D. D., Barro, G., Faber, S. M., Dekel, A., Somerville, R. S., Young, J. A., Williams, C. C., McIntosh, D. H., Georgakakis, A., Hasinger, G., Nandra, K., Civano, F., Alexander, D. M., Almaini, O., Conselice, C. J., Donley, J. L., Ferguson, H. C., Giavalisco, M., Grogin, N. A., Hathi, N., Hawkins, M., Koekemoer, A. M., Koo, D. C., McGrath, E. J., Mobasher, B., Pérez González, P. G., Pforr, J., Primack, J. R., Santini, P., Stefanon, M., Trump, J. R., van der Wel, A., Wuyts, S., & Yan, H. 2017, ApJ, 846, 112

Martin, C. L., Shapley, A. E., Coil, A. L., Kornei, K. A., Bundy, K., Weiner, B. J., Noeske, K. G., & Schiminovich, D. 2012, ApJ, 760, 127

Moster, B. P., Naab, T., & White, S. D. M. 2013, MNRAS, 428, 3121

Newman, S. F., Genzel, R., Förster Schreiber, N. M., Shapiro Griffin, K., Mancini, C., Lilly, S. J., Renzini, A., Bouché, N., Burkert, A., Buschkamp, P., Carollo, C. M., Cresci, G., Davies, R., Eisenhauer, F., Genel, S., Hicks, E. K. S., Kurk, J., Lutz, D., Naab, T., Peng, Y., Sternberg, A., Tacconi, L. J., Vergani, D., Wuyts, S., & Zamorani, G. 2012, ApJ, 761, 43

Pettini, M., Ellison, S. L., Steidel, C. C., Shapley, A. E., & Bowen, D. V. 2000, ApJ, 532 65

Pettini, M., Shapley, A. E., Steidel, C. C., Cuby, J.-G., Dickinson, M., Moorwood, A. F. M., Adelberger, K. L., & Giavalisco, M. 2001, ApJ, 554, 981

Rupke, D. S. N. & Veilleux, S. 2011, ApJL, 729, L27

Rupke, D. S. N. & Veilleux, S. 2013, ApJ, 768, 75

Rupke, D. S. N., Coil, A. Geach, J. E., Tremonti, C., Diamond-Stanic, A. M., George, E. R., Hickox, R. C., Kepley, A. A., Leung, G., Moustakas, J., Rudnick, G., & Sell, P. H. 2019, Nature, 574, 7780

Sanders, R. L., Shapley, A. E., Kriek, M., Reddy, N. A., Freeman, W. R., Coil, A. L., Siana, B., Mobasher, B., Shivaei, I., Price, S. H., & de Groot, L. 2015, ApJ, 799, 138

Sanders, R. L., Shapley, A. E., Kriek, M., Reddy, N. A., Freeman, W. R., Coil, A. L., Siana, B., Mobasher, B., Shivaei, I., Price, S. H., & de Groot, L. 2016, ApJ, 816, 23

Sell, P. H., Tremonti, C. A., Hickox, R. C., Diamond-Stanic, A. M., Moustakas, J., Coil, A., Williams, A., Rudnick, G., Robaina, A., Geach, J. E., Heinz, S., & Wilcots, E. M. 2014, MNRAS, 441, 3417

Shapley, A. E., Steidel, C. C., Pettini, M., & Adelberger, K. L. 2003, ApJ, 588, 65

Stefanon, M., Marchesini, D., Rudnick, G. H., Brammer, G. B., & Whitaker, K. E. 2013, ApJ, 768, 92

Steidel, C. C., Giavalisco, M., Pettini, M., Dickinson, M., & Adelberger, K. L. 1996, ApJ, 462, L17

Steidel, C. C., Erb, D. K., Shapley, A. E., Pettini, M., Reddy, N., Bogosavljevic, M., Rudie, G. C., & Rakic, O. 2010, ApJ, 717, 289

Tremonti, C. A., Moustakas, J., & Diamond-Stanic, A. M. 2007, ApJ, 663, L77

van der Wel, A., Franx, M., van Dokkum, P. G., Skelton, R. E., Momcheva, I. G., Whitaker, K. E., Brammer, G. B., Bell, E. F., Rix, H.-W., Wuyts, S., Ferguson, H. C., Holden, B. P., Barro, G., Koekemoer, A. M., Chang, Y.-Y., McGrath, E. J., Häussler, B., Dekel, A., Behroozi, P., Fumagalli, M., Leja, J., Lundgren, B. F., Maseda, M. V., Nelson, E. J., Wake, D. A., Patel, S. G., Labbé, I., Faber, S. M., Grogin, N. A., & Kocevski, D. D. 2014, ApJ, 788, 28

van Dokkum, P. G., Franx, M., Kriek, M., Holden, B., Illingworth, G. D., Magee, D., Bouwens, R., Marchesini, D., Quadri, R., Rudnick, G., Taylor, E. N., & Toft, S. 2008, ApJ, 677, L5

van Dokkum, P. G., Leja, J., Nelson, E. J., Patel, S., Skelton, R. E., Momcheva, I., Brammer, G., Whitaker, K. E., Lundgren, B., Fumagalli, M., Conroy, C., Förster Schreiber, N., Franx, M., Kriek, M., Labbé, I., Marchesini, D., Rix, H.-W., van der Wel, A., & Wuyts, S. 2013, ApJL, 771, L35

van Dokkum, P. G., Nelson, E. J., Franx, M., Oesch, P., Momcheva, I., Brammer, G., Förster Schreiber, N. M., Skelton, R. E., Whitaker, K. E., van der Wel, A., Bezanson, R., Fumagalli, M., Illingworth, G. D., Kriek, M., Leja, J., & Wuyts, S. 2015, ApJ, 813, 23

Weiner, B. J., Coil, A. L., Prochaska, J. X., Newman, J. A., Cooper, M. C., Bundy, K., Conselice, C. J., Dutton, A. A., Faber, S. M., Koo, D. C., Lotz, J. M., Rieke, G. H., & Rubin, K. H. R. 2009, ApJ, 692, 187

Werk, J. K., Prochaska, J. X., Tumlinson, J., Peeples, M. S., Tripp, T. M., Fox, A. J., Lehner, N., Thom, C., O'Meara, J. M., Ford, A. B., Bordoloi, R., Katz, N., Tejos, N., Oppenheimer, B. D., Davé, R., & Weinberg, D. H. 2014, 792, 8

Zirm, A. W., van der Wel, A., Franx, M., Labbé, I., Trujillo, I., van Dokkum, P., Toft, S., Daddi, E., Rudnick, G., Rix, H.-W., Röttgering, H. J. A., & van der Werf, P. 2007, ApJ, 656, 66